Response of Monsoon Rainfall to Changes in the Latitude of the Equatorward Coastline of a Zonally Symmetric Continent

KATRINA L. HUI[a] AND SIMONA BORDONI[b,a]

[a] *Environmental Science and Engineering, California Institute of Technology, Pasadena, California*
[b] *Department of Civil, Environmental and Mechanical Engineering, University of Trento, Trento, Italy*

(Manuscript received 21 April 2020, in final form 28 January 2021)

ABSTRACT: Recent studies have shown that the rapid onset of the monsoon can be interpreted as a switch in the tropical circulation, which can occur even in the absence of land–sea contrast, from a dynamical regime controlled by eddy momentum fluxes to a monsoon regime more directly controlled by energetic constraints. Here we investigate how one aspect of continental geometry, that is, the position of the equatorward coastal boundary, influences such transitions. Experiments are conducted with an aquaplanet model with a slab ocean, in which different zonally symmetric continents are prescribed in the Northern Hemisphere poleward from southern boundaries at various latitudes, with ''land'' having a mixed layer depth two orders of magnitude smaller than ocean. For continents extending to tropical latitudes, the simulated monsoon features a rapid migration of the convergence zone over the continent, similar to what is seen in observed monsoons. For continents with more poleward southern boundaries, the main precipitation zone remains over the ocean, moving gradually into the summer hemisphere. We show that the absence of land at tropical latitudes prevents the rapid displacement into the subtropics of the maximum in lower-level moist static energy and, with it, the establishment of an overturning circulation with a subtropical convergence zone that can transition rapidly into an angular momentum–conserving monsoon regime.

KEYWORDS: Atmospheric circulation; Dynamics; Hadley circulation; Hydrologic cycle; Meridional overturning circulation; Momentum; Monsoons

1. Introduction

The monsoon is a prominent climatological phenomenon of the summertime circulation that dominates the annual cycle over much of the tropics and subtropics. It brings abundant rainfall to regions that feature otherwise very arid winters, so its onset, strength, and variability have large socioeconomic impacts. All regional monsoons are characterized by rainfall largely confined to the warm season, with accompanying circulation changes.

In disagreement with traditional views of monsoons as large-scale sea-breeze circulations, understanding has recently emerged and led to novel consideration of these systems as intimately tied to the tropical overturning circulation and associated intertropical convergence zone (ITCZ). In fact, monsoons are now widely viewed as broad, cross-equatorial Hadley circulations that are energetically direct and export energy away from their ascending branches (e.g., Biasutti et al. 2018) and that project strongly on the global zonal mean (e.g., Walker and Bordoni 2016; Walker 2017). According to this emerging view, monsoons are a manifestation of the seasonal excursion of the ITCZ into the summer hemisphere subtropical continents. In this respect, theories that have been developed for the understanding of the Hadley cell and its response to perturbations by different forcings and on different time scales might be applicable, at least to some extent, to the understanding of monsoons.

Key to this advanced understanding have been theoretical constraints on tropical overturning circulations dictated by large-scale budgets of angular momentum (AM) (e.g., Held and Hou 1980; Lindzen and Hou 1988; Plumb and Hou 1992; Privé and Plumb 2007a) and energy (e.g., Neelin and Held 1987; Chou and Neelin 2004; Neelin 2007; Kang et al. 2008, 2009) and highly idealized modeling studies, including aquaplanets. For instance, in simulations with idealized general circulation models (GCM) with a seasonal cycle and no zonal asymmetries, Schneider and Bordoni (2008) and Bordoni and Schneider (2008) showed that the rapid onset of the monsoon might be interpreted as a switch between a dynamical regime where the tropical circulation strength is controlled by eddy momentum fluxes (Walker and Schneider 2006) and a monsoon regime where the circulation approaches AM conservation and its strength is more directly controlled by energetic constraints, which causes the monsoonal cross-equatorial cell to grow rapidly in strength and poleward extent. This switch can happen even in the absence of surface inhomogeneities, provided that the lower boundary has low enough thermal inertia. The sensitivity of the transition rate and latitudinal extent to year length, lower-boundary thermal inertia, and rotation rate was more recently explored by Geen et al. (2018, 2019). Additionally, Geen et al. (2018) provide a complimentary view to the AM budget by focusing on the vorticity budget and finding that this transition can also be thought of as a rapid reduction in the upper-level absolute vorticity within the tropical circulation due to positive horizontal advection and negative vortex stretching tendencies.

AM conservation by a circulation in the monsoon regime, together with thermal wind balance, requires that the circulation boundary be located in a region of zero vertical wind shear, where free-tropospheric temperatures maximize (Lindzen and Hou 1988). For a moist atmosphere in convective

Corresponding author: Katrina L. Hui, klhui@caltech.edu

DOI: 10.1175/JAS-D-20-0110.1

quasi equilibrium (CQE), in which convection maintains a moist adiabatic temperature profile and upper-tropospheric temperatures covary with the subcloud moist static energy (MSE) (e.g., Emanuel et al. 1994), the circulation boundary will have to be co-located with the maximum in lower-level MSE (e.g., Emanuel 1995; Privé and Plumb 2007a). In other words, dynamical constraints from AM conservation together with thermodynamic constraints imposed by convection yield a strong coupling between the circulation and the distribution of lower-level MSE. While not prognostic, given that the circulation itself influences the MSE distribution, the resulting relationship has proved very powerful in allowing for a mechanistic understanding of how factors such as land geometry, orography, albedo, and ocean fluxes impact the monsoonal rainfall through their impact on the MSE distribution. For instance, it has led to a reinterpretation of the role of topography in the South Asian monsoon: long considered necessary to drive a strong monsoon through elevated heating (Flohn 1957), topography is now recognized as a mechanical insulator, preventing mixing between cold and dry extratropical air and the moist and warm monsoonal air (Boos and Kuang 2010; Molnar et al. 2010).

An alternative framework that has also allowed for significant progress in the understanding of the zonally averaged Hadley cell and the ITCZ has been based on the atmospheric energy budget, which interprets the ITCZ response as part of the meridional energy fluxes necessary to restore energy balance to a given perturbation (Kang et al. 2008; Bischoff and Schneider 2014). While the extension of this framework to zonally asymmetric circulations, such as monsoons, remains an area of active research (e.g., Boos and Korty 2016; Adam et al. 2016), constraints that apply to the zonal mean could also prove useful to regional monsoons (e.g., Schneider et al. 2014). See Hill (2019) for a review of merits of and outstanding challenges in energy-based theories of monsoons.

In this work, we aim to understand how simple aspects of continental geometry influence the fundamental dynamics of monsoonal circulations building on more idealized work. As argued by recent studies (Jeevanjee et al. 2017; Collins et al. 2018), approaches in which complexity is increased progressively allow for understanding of fundamental dynamics in the absence of other complicating but poorly understood factors. Although uniform mixed layer depth (MLD) aquaplanet studies have provided great understanding of how MLD may affect the monsoon dynamical transition rate (Bordoni and Schneider 2008; Geen et al. 2018, 2019), in this work we take a step toward realism by introducing meridional asymmetry in the lower boundary. Expanding on the work of Laraia (2015), who introduced a zonally symmetric continent in the Northern Hemisphere (NH) with a southern boundary at 10°N in an aquaplanet GCM with idealized physics, we run the same model with five different zonally symmetric configurations of NH land that extends poleward from southern boundaries at various latitudes to vary the hemispheric asymmetry in thermal inertia. Similar approaches were taken in models with more realistic physics (e.g., Dirmeyer 1998; Xie and Saiki 1999; Chou et al. 2001). Here we attempt to fill the gap between idealized aquaplanet GCMs and comprehensive models. This approach was recently taken by Zhou and Xie (2018), who used a GCM similar to the one used here to study the effects of land albedo, continental extent, and soil moisture on the monsoon through their influence on near-surface equivalent potential temperature (and hence MSE). Relevant to this study is the finding that the monsoon weakens significantly as the equatorward coastal boundary is displaced poleward. Similar goals also motivated the Tropical Rain belts with an Annual cycle and a Continent Model Intercomparison Project (TRACMIP; Voigt et al. 2016). What distinguishes our work from these previous studies is the use of just one model to study the response of both monsoon onset timing and spatial distribution to systematic changes in one aspect of continental configuration (position of the equatorward coastal boundary) and the dynamical perspective provided by analyses of associated changes in the AM and vorticity budgets. Section 2 describes the idealized GCM and simulations used in this study, as well as the monsoon onset indices. Section 3 focuses on the seasonal cycle of precipitation in the different experiments, while section 4 interprets these results using dynamical constraints from the AM and the vorticity budgets. Discussion and conclusions follow in sections 5 and 6, respectively.

2. Methods and tools

a. Idealized GCM

A moist idealized aquaplanet GCM based on the Geophysical Fluid Dynamics Laboratory (GFDL) Flexible Modeling System (Frierson et al. 2006; O'Gorman and Schneider 2008) is used, which solves the primitive equations of motion on a sphere with Earth's radius.

The lower boundary of the model consists of a slab ocean, with sea surface temperatures (T_s) evolving according to the surface energy budget:

$$c\rho d\frac{\partial T_s}{\partial t} = O_s = S^s - L^s - \mathrm{LH} - \mathrm{SH} - \nabla\cdot\mathbf{F}_0, \qquad (1)$$

with ocean heat storage O_s on the left-hand side, with water specific heat c, density ρ, and MLD d, being balanced by radiative and turbulent energy fluxes into the surface (with net incoming shortwave flux S^s, net outgoing longwave flux L^s, outgoing sensible and latent heat fluxes, respectively, SH and LH) and any energy flux convergence by ocean currents ($-\nabla\cdot\mathbf{F}_0$, also known as Q flux). Land and ocean only differ in the corresponding MLD d, which we choose as 0.2 m for land and 20 m for ocean. A two-stream gray radiation scheme is used where the optical depth is prescribed. While a diurnal cycle is not included, the GCM is forced by a seasonal cycle of insolation with a 360-day Julian year, using realistic Earthlike values of obliquity and solar constant of 23.5° and 1360 W m^{-2}, respectively, but zero eccentricity. The GCM includes an active hydrological cycle, where precipitation can form by either large-scale condensation or convection following a simplified Betts–Miller convection scheme as in Frierson (2007). Since precipitation is assumed to fall out immediately, there is no liquid water or ice in the atmosphere, hence no clouds. To compensate for the lack of clouds, we use a spatially uniform surface albedo of $\alpha = 0.38$. With these simplifications, this GCM

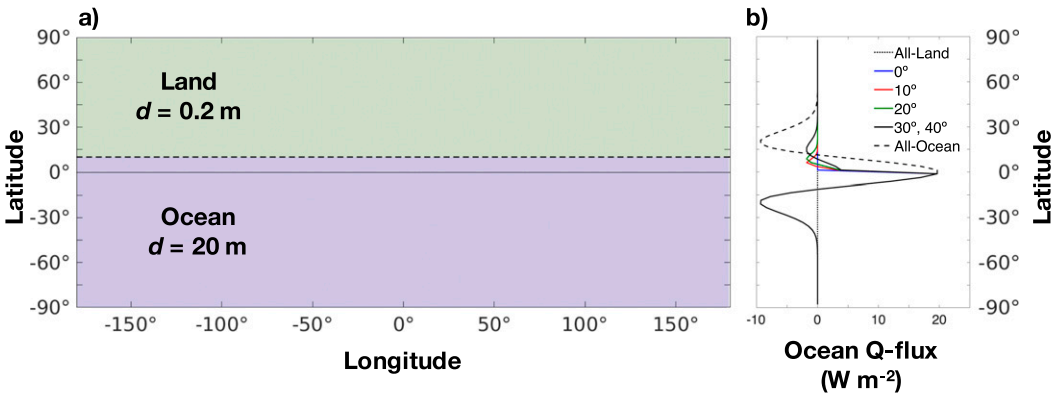

FIG. 1. Model setup: (a) schematic of continental configuration for the 10° simulation, where land and ocean have mixed layer depths of 0.2 and 20 m, respectively, and (b) the ocean Q flux distributions for each simulation.

does not account for important climate feedbacks such as surface albedo, cloud, or radiative water vapor feedbacks, but nonetheless well resolves tropical and extratropical circulations, their mutual interactions, and their impact on the hydrological cycle.

For this study, we perform five simulations with an idealized continent. The model is run with fully saturated NH land (d = 0.2 m) that extends poleward from southern boundaries at 0°, 10°, 20°, 30°, and 40° (Fig. 1a), with ocean MLD d = 0.2 m. Two uniform MLD aquaplanet simulations were also run: one with all land (d = 20 m everywhere) and one with all ocean (d = 20 m everywhere), to which we will refer to as the all-land and the all-ocean cases, respectively. For each simulation, the ocean energy transport is prescribed through the ocean Q flux term in Eq. (1) following the zonally symmetric and time-invariant form in Merlis et al. (2013):

$$\nabla \cdot \mathbf{F}_0(\phi) = \begin{cases} Q_{\mathrm{NH}} \dfrac{1}{\cos\phi}\left(1 - \dfrac{2\phi^2}{\phi_{\mathrm{NH}}^2}\right) \exp\left(\dfrac{-\phi^2}{\phi_{\mathrm{NH}}^2}\right), & \text{if} \quad \phi > 0 \\ Q_{\mathrm{SH}} \dfrac{1}{\cos\phi}\left(1 - \dfrac{2\phi^2}{\phi_{\mathrm{SH}}^2}\right) \exp\left(\dfrac{-\phi^2}{\phi_{\mathrm{SH}}^2}\right), & \text{if} \quad \phi < 0. \end{cases} \tag{2}$$

In the all-ocean simulation, we used $Q_{\mathrm{NH}} = Q_{\mathrm{SH}} = 20$ and widths $\phi_{\mathrm{NH}} = \phi_{\mathrm{SH}} = 16°$. For each simulation including land, Q_{NH} and ϕ_{NH} are varied (Table 1) so that the ocean heat transport (OHT; the meridional integral of the Q flux) approaches zero at the coastline (Fig. 1b). Consistently, it is zero everywhere in the all-land simulation. Every simulation was performed with T42 horizontal spectral resolution with 30 vertical levels and run for 20 years, with data from the last 10 years used in the analyses shown below. Since our model uses a zonally symmetric setup, all fields presented in this study are global zonal averages. Because land and ocean differ only by their MLD, the only aspect of the land–sea contrast we account for is the capability of the ocean to store and transport energy due to its higher thermal inertia and prescribed ocean Q flux.

b. Monsoon onset metrics

To quantitatively analyze the influence of continental geometry on the monsoon onset timing, we calculate monsoon onset using two methods. The first identifies onset as the pentad at which the mean tropical precipitation (averaged over 10° to 30°) first exceeds its annual mean, similar to Zhou and Xie (2018) and to which we refer to as the ZX18 index. We also calculate onset following the method described in Walker and Bordoni (2016), to which we refer to as the WB16 index. The WB16 index is based on detecting the changepoint of a two-phase linear regression of the cumulative moisture flux convergence (CMFC) over a representative region (here taken as the latitudinal band between 10° and 30°, Fig. 3). Because the moisture flux convergence primarily balances net precipitation, this index detects onset as the time at which net precipitation switches from negative to positive (and withdrawal as the opposite transition).

3. Seasonal cycle

In this study we regard the monsoon as excursions into subtropical latitudes of the ITCZ embedded within the ascending branch of the cross-equatorial Hadley cell. In this section, we begin by reviewing the observed seasonal cycle of the precipitation and the circulation and we then explore how well energetic predictors capture this evolution.

a. Temporal structure

The seasonal cycle of precipitation from each simulation with idealized continent and the all-ocean case is depicted in Fig. 2 (color contours). Here, and in most of the following figures, results from the all-land simulation are not shown

TABLE 1. Q-flux amplitudes and widths used for each simulation.

Simulation	Q_{NH}	ϕ_{NH}	Q_{SH}	ϕ_{SH}
Land	0	16°	0	16°
0°	0	5°	20	16°
10°	4	5°	20	16°
20°	4	7°	20	16°
30°	4	12°	20	16°
40°	4	12°	20	16°
Ocean	20	16°	20	16°

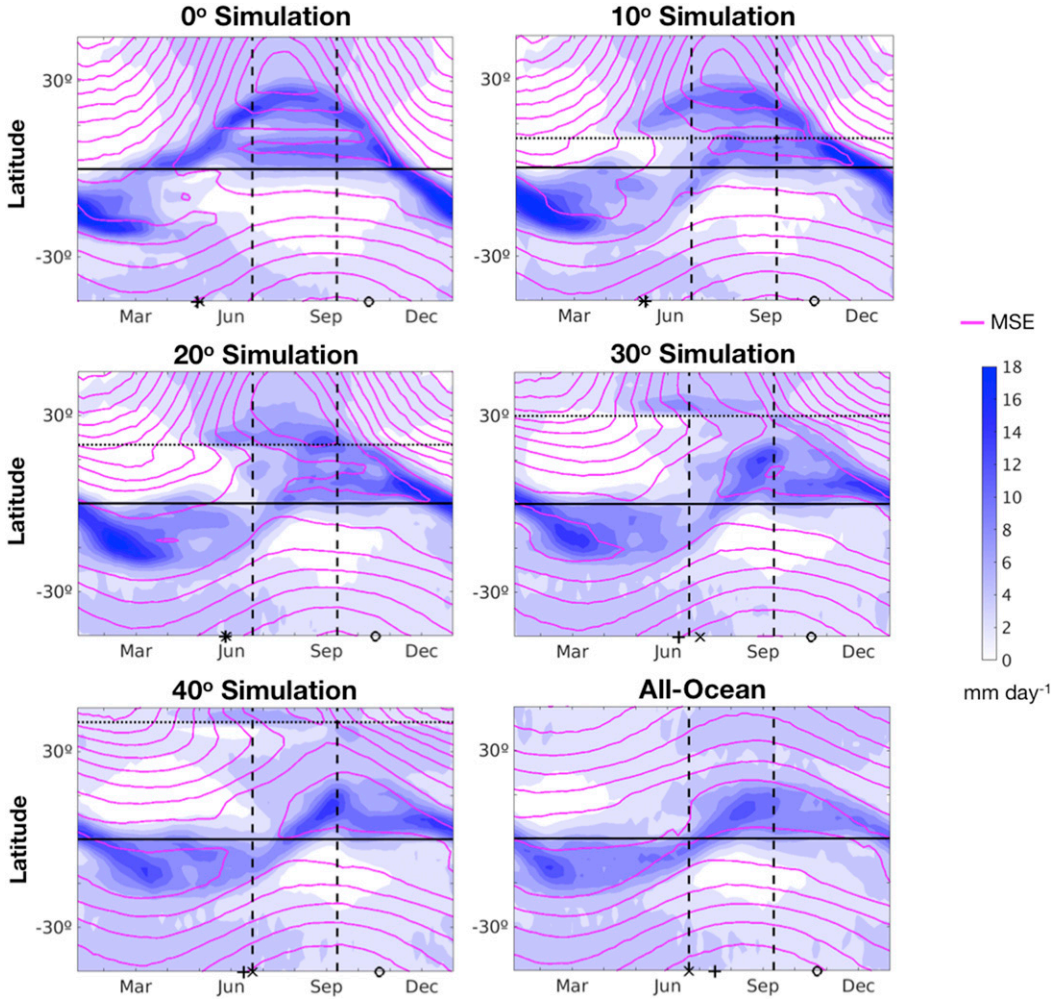

FIG. 2. Seasonal cycles from simulations with southern boundaries of land at 0°, 10°, 20°, 30°, and 40° and the all-ocean aquaplanet. Color contours indicate precipitation (contour interval: 2 mm day^{-1}). Magenta contours indicate near-surface MSE taken at $\sigma = 0.887$ (contour interval: 8×10^3 J kg^{-1}). The equator is marked in a solid horizontal black line and the southern boundary of land in each simulation is shown in a dotted horizontal black line. The dashed vertical lines mark 21 Jun and 11 Sep, used in the analysis for Figs. 6–8. The black × symbols indicate monsoon onset as calculated in Zhou and Xie (2018), while the black plus signs and the black circles indicate monsoon onset and retreat as calculated in Walker and Bordoni (2016).

because they are similar to those discussed in earlier studies (Bordoni and Schneider 2008; Geen et al. 2018, 2019). Some important statistics and metrics from this case are however presented below. Overall, the precipitation temporal structure in simulations with land extending into the tropics northward of 0°, 10°, and 20° all have a similar asymmetry, characterized by a rapid cross-equatorial jump of the ITCZ from the Southern Hemisphere (SH) into the NH during NH spring and a slower retreat back to the SH in NH fall—this behavior is similar to that seen within observed monsoons. In contrast, the 30° and 40° simulations look generally similar to the all-ocean simulation, with a relatively smooth ITCZ progression.

In addition to the gross behavior described above, some interesting and unexpected features arise from the inclusion of a simple hemispheric asymmetry in MLD. More specifically, the heating over land at the beginning of the NH warm season gives rise to a coastal precipitation maximum in every simulation. In simulations with land extending deeper in the tropics, such as the 0° and 10° simulations, this coastal precipitation maximum does not appear as distinct from the main convergence zone of the cross-equatorial Hadley cell, which, thanks to mechanisms described in section 4, can migrate rapidly into subtropical latitudes. Notice for instance the covariation of the precipitation and the zero contour of the lower-level mass streamfunction in these two simulations (top panels of Figs. 2 and 4). As land is moved farther poleward, as for instance in the 30° and 40° simulations, the two maxima become more separate, with no association between the ascending branch of the Hadley cell and the coastal precipitation maximum (Figs. 2 and 4). What drives the coastal precipitation maximum? We

TABLE 2. Dates of monsoon onset and retreat, as calculated in Walker and Bordoni (2016).

Simulation	Onset	Retreat
Land	1 May	16 Oct
0°	1 May	11 Oct
10°	6 May	16 Oct
20°	26 May	16 Oct
30°	11 Jun	16 Oct
40°	11 Jun	21 Oct
Ocean	16 Jul	21 Oct

answer this question by analyzing the fraction of precipitation P due to moisture flux convergence, calculated as $(P - E)/P$, where E is evaporation: a fraction lower (larger) than 50% indicates that P is primarily driven by local evaporation (moisture flux convergence by the large-scale circulation). In the 10° simulation, this ratio is ~30% during early summer, and increases to ~70% during the peak of the summer. In the 40° simulation, this ratio never exceeds 20% at the coastal precipitation maximum. We recognize that these secondary precipitation maxima are artifacts of using a fully saturated surface in our model. Future work will include further steps toward realism by, for instance, limiting evaporation over land (e.g., Voigt et al. 2016).

Continental geometry also affects the timing of monsoon onset, which, according to both indices used here, tends to become increasingly delayed as the continent southern boundary is moved farther poleward, varying over a span of 2 months across all simulations (Table 2). Interestingly, the timing of monsoon retreat is less sensitive to the position of the coastal boundary, varying over the span of 10 days. One of the advantages of the WB16 index is that it also gives some insight into the rapidity of monsoon onset: as seen in Fig. 3, in the simulations with southern boundary equatorward of 20°, the rate of CMFC increase after monsoon onset strengthens rapidly, as the circulations intensifies quickly and so does the moisture flux convergence in the tropical region. In contrast, the 30°, 40°, and all-ocean simulations show relatively more gradual changes in the CMFC, reflective of less rapid changes in the circulation.

The near-surface MSE distribution (magenta lines in Fig. 2) shows similar features as the precipitation distribution, in agreement with expectations from CQE (e.g., Emanuel 1995; Privé and Plumb 2007a). The 0°, 10°, and 20° simulations show an abrupt poleward jump in the MSE maximum that coincides with the rapid ITCZ transition during NH spring. An interesting double-maxima structure is also observed during the monsoon from July to September when there is also a double ITCZ. The transition during NH fall is much more gradual. Like in the precipitation distributions, the near-surface MSE transitions in the 30°, 40°, and all-ocean experiments are relatively smoother.

To explore how these precipitation patterns reflect on circulation patterns, Fig. 4 shows the seasonal cycles of the lower-level ($\sigma = 0.887$) zonal mean mass streamfunction and zonal wind (u_{low}). In each simulation, the ascending branch of the streamfunction closely follows the precipitation maximum (Fig. 2), where a more asymmetric temporal structure

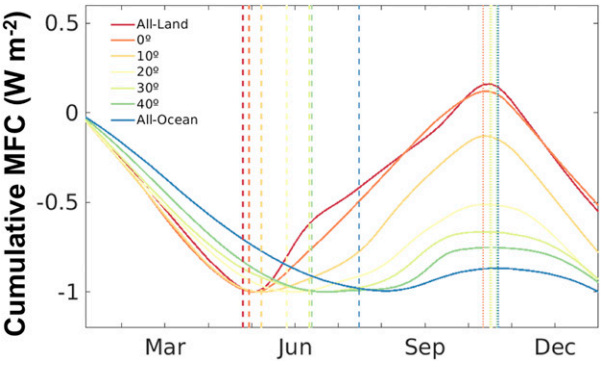

FIG. 3. Cumulative moisture flux convergence mean (10°–30°N), normalized by the minimum for each simulation, from which the monsoon onset and retreat indices are calculated as in Walker and Bordoni (2016). Resulting monsoon onset (dashed) and retreat (dotted) indices are listed in Table 2.

and farther poleward extent are observed in the 0°, 10°, and 20° simulations relative to those of the 30°, 40°, and all-ocean simulations. At monsoon onset in the 0°, 10°, and 20° simulations we observe a rapid establishment and intensification of lower-level westerlies from around the equator to the cross-equatorial Hadley cell's poleward boundary, compared to a relatively weaker and delayed onset of westerlies in the 30°, 40°, and all-ocean simulations. The establishment of lower-level westerly flow primarily results because the dominant zonal momentum budget in the boundary layer is a balance between the Coriolis force and friction. Westerlies must hence develop whenever northward (southward) meridional flow exists in the NH (SH) (cf. Schneider and Bordoni 2008). In the simulations with land extending to lower latitudes, the rapid intensification of the summer westerlies is in fact concomitant with the rapid increase in lower-level meridional winds and rapid growth in the extent of the winter Hadley cell at monsoon onset (Fig. 4, also see Fig. 6). In contrast, the summer westerlies in the simulations with land located farther poleward remain weaker and more confined to the tropics, and also intensify later in the season, consistent with a more slowly growing winter Hadley cell that does not extend as far poleward into the summer hemisphere.

b. *Connection between the ITCZ and the energetics*

While several ITCZ metrics exist in the literature, here we identify the ITCZ as the location of the precipitation maximum. We recognize that one single parameter does not capture the complexity of the precipitation distribution (Popp and Lutsko 2017), but this metric captures the most important trends discussed below. We also calculate three ITCZ predictors: the maximum in lower-level MSE (MSE_{max}; Privé and Plumb 2007a), the latitude of vanishing total energy transport, the energy flux equator (EFE) (e.g., Kang et al. 2008), and its analytical approximation (cf. Bischoff and Schneider 2014)

$$\delta \approx -\frac{1}{a}\frac{\langle \overline{vh} \rangle_0}{\partial_y \langle \overline{vh} \rangle_0} = -\frac{1}{a}\frac{\langle \overline{vh} \rangle_0}{\overline{\text{NEI}}_0}, \tag{3}$$

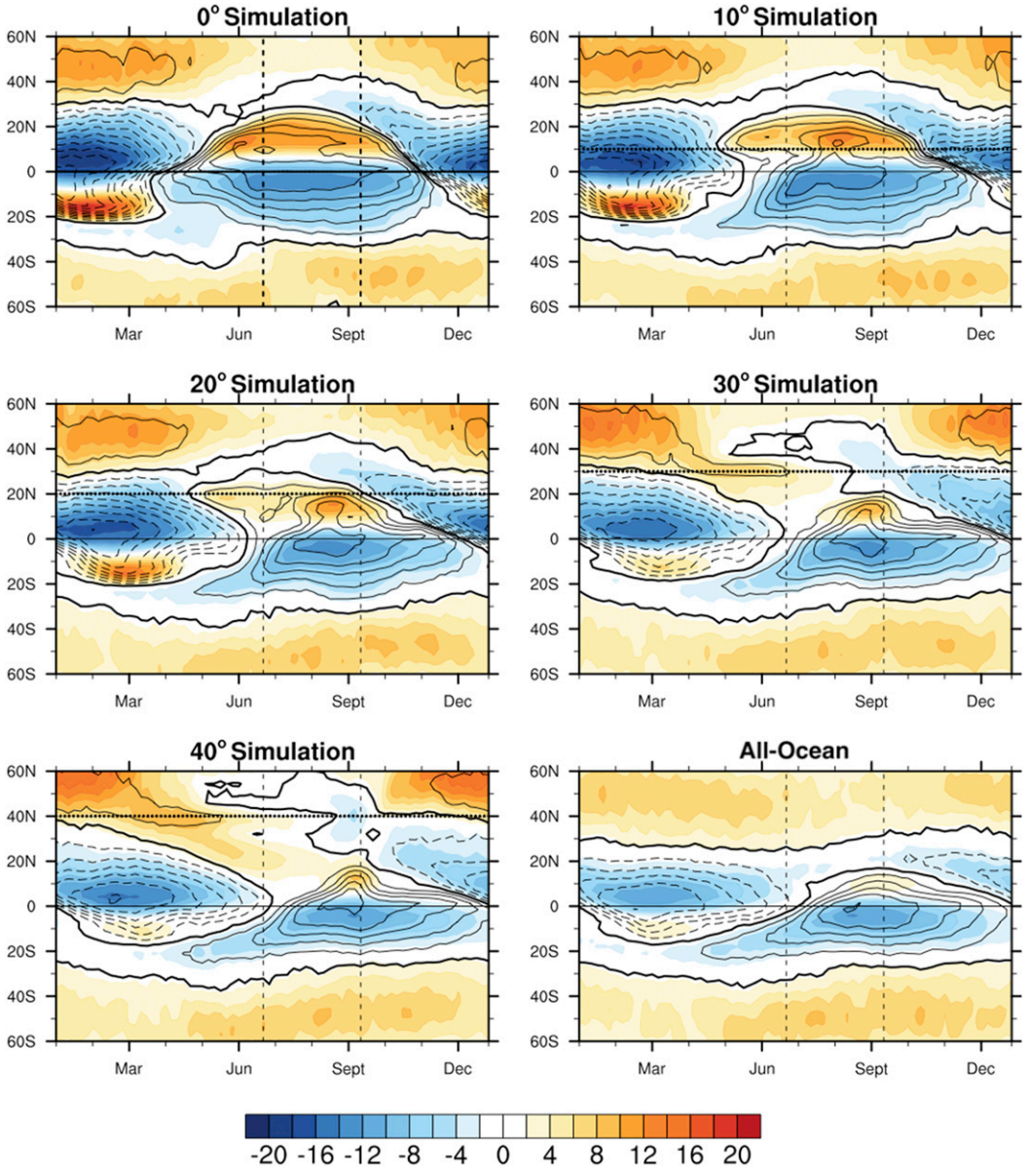

FIG. 4. Seasonal cycle of the lower-level mass streamfunction and zonal wind from simulations with southern boundaries of land at 0°, 10°, 20°, 30°, and 40° and the all-ocean aquaplanet. Color contours indicate lower-level (σ = 0.887) zonal wind (contour interval: 2 m s^{-1}). Black contours mark the lower-level mass streamfunction Ψ_{low} (counterclockwise in solid, clockwise in dashed; contour interval: 40 $\times$ 10^9 kg s^{-1}; zero contour in bold). The equator, southern boundary of the continent, and 21 Jun and 11 Sep are marked as in Fig. 2.

where δ is the EFE, $\langle vh \rangle$ is the vertically integrated meridional MSE transport and NEI is the net energy input into the atmospheric column (equaling the difference between TOA radiative fluxes and surface radiative and turbulent enthalpy fluxes). The subscript 0 indicates quantities evaluated at the equator, $\overline{(\cdot)}$ is the time and zonal mean, and a is Earth's radius. We refer to δ as BS14. Averages of the ITCZ and all three predictors are taken over both solstitial seasons to see how changing hemispheric asymmetry in thermal inertia can affect the ITCZ poleward migration. Given the differences in monsoon onset and withdrawal timing across simulations, these solstitial averages are computed over 15-pentad time intervals centered around the time of maximal excursion.

Not surprisingly, continental geometry strongly impacts the rainfall poleward extent (Fig. 5). In the simulations with NH land, while the magnitudes of the ITCZ and predictors vary slightly, they agree well on two main general trends. First, during both NH summer and SH summer, the poleward extent of the ITCZ decreases as the southern boundary of the continent is moved farther poleward and the hemispheric asymmetry in

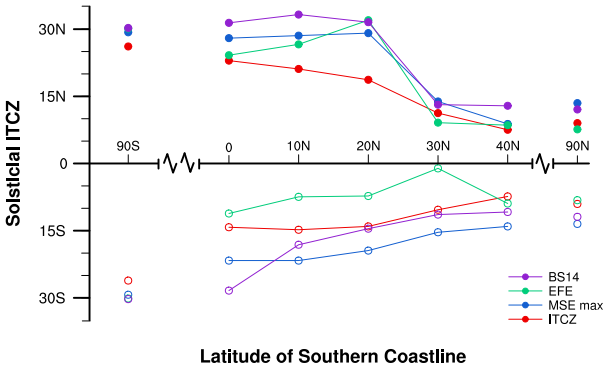

FIG. 5. Solstitial (NH summer in filled circles and SH summer in open circles) ITCZ position (red), near-surface MSE maximum (blue), EFE (green), and first-order estimate of EFE from BS14 (purple) for all simulations. Note the discontinuities in the x axis.

thermal inertia is decreased. Second, in each simulation, the NH summer ITCZ tends to extend farther poleward than the SH summer ITCZ. This asymmetry decreases as the continent is moved farther from the equator. For example, the NH summer ITCZ extends ~9° farther poleward than the SH summer ITCZ in the 0° simulation, but only ~1° in the 30° simulation. No asymmetry is seen in the 40° case. The hemispheric asymmetry in NEI arising from the introduction of NH land in the tropics, therefore, results in a larger poleward excursion of the summertime ITCZ. In this respect, land–sea contrast matters to the extent it can push the ITCZ far enough off the equator, in association with Hadley circulations that become more strongly cross equatorial.

Figure 5 also shows the different ITCZ metrics for the all-land and all-ocean simulations. A comparison between the all-land and the 0° simulations highlights the impact of hemispheric asymmetry in the surface thermal inertia: while the two cases have similar ITCZ locations in NH summer, the ocean in the SH in the 0° simulation prevents the ITCZ from moving as far poleward during SH summer. Interestingly, in the all-ocean simulation the poleward extent of the NH summer and SH summer ITCZs is slightly larger than what is seen in the 40°. This might be because in the all-ocean simulation, precipitation maxima with wider latitudinal ranges but lower intensities are observed during NH summer and SH summer relative to the those observed in the 40° simulations (Fig. 2), allowing slightly more poleward solstitial ITCZs.

From the results presented above, only the simulations with land extending from the north pole down to 0°, 10°, and 20° and the all-land case are able to reproduce the rapid cross-equatorial jump of the ITCZ and reversal of zonal winds characteristic of the monsoon. The energetic framework allows us to interpret these results, at least in terms of seasonally averaged ITCZ metrics, through the impact of the landmasses on the interhemispheric asymmetry in NEI into the atmospheric column. More in depth analysis of the seasonal evolution of the EFE in relation to energetic changes is left for future work.

4. Role of dynamics

To better understand the mechanisms that drive the seasonal changes described in section 3, we look more closely at the overturning circulation to relate its seasonal transitions to recent monsoon dynamical theories (Schneider and Bordoni 2008; Bordoni and Schneider 2008; Geen et al. 2018).

a. Angular momentum budget perspective

Schneider and Bordoni (2008) and Bordoni and Schneider (2008) showed that the rapidity of monsoon transitions in idealized aquaplanet simulations can be explained as a switch between two dynamical regimes that differ in the amount of influence eddy momentum fluxes have on the strength of the tropical circulation. The leading-order balance in the zonally averaged steady-state zonal momentum budget in the upper branch of the circulation, where friction and vertical advection can be neglected, is

$$(f+\overline{\zeta})\overline{v} = f(1-R_o)\overline{v} \approx \mathcal{S}, \tag{4}$$

with planetary vorticity $f = 2\Omega\sin\phi$, relative vorticity $\overline{\zeta} = -\partial\overline{u}/\partial y$, meridional wind v, local Rossby number $R_o = -\overline{\zeta}/f$, and transient eddy momentum flux divergence (EMFD) $\mathcal{S} = \partial\overline{u'v'}/\partial y + \partial\overline{u'\omega'}/\partial p$, where u is the zonal velocity, ω is the vertical pressure velocity, p is pressure, and $(\cdot)' = (\cdot) - \overline{(\cdot)}$ is the deviation from the time mean. While all quantities are expressed in Cartesian coordinates for simplicity, both the model and our calculations below are in spherical coordinates. As discussed in Schneider (2006), R_o is a measure of how far (small R_o) or close (R_o approaching 1) the circulation is from the angular momentum–conserving (AMC) limit. In the first case, that is, $R_o \to 0$, Eq. (4) reduces to $f\overline{v} \approx \mathcal{S}$. In this regime, AM contours are vertical and the strength of the mean meridional circulation ($\overline{v}$) is tied to the EMFD. When $R_o \to 1$, the meridional AM gradient following the streamlines in the upper branch of the circulation approaches zero, and Eq. (4) becomes a trivial balance, no longer providing constraints on the circulation strength. In this limit, hence, the circulation responds more directly to the thermal forcing (Held and Hou 1980; Lindzen and Hou 1988). Bordoni and Schneider (2008) and Schneider and Bordoni (2008) demonstrated that the rapid monsoon-like transition of the ITCZ into the subtropics seen in simulations with a uniform lower boundary with low thermal inertia coincides with a rapid switch of the circulation from the eddy-driven into the AMC regime.

How does the presence or absence of land in the tropics and subtropics affect these transitions? And how does changing the hemispheric asymmetry in thermal inertia influence their timing and rapidity, by for instance favoring or disfavoring the relative influence of eddies on the strength of the meridional overturning circulation (MOC) at different times of the seasonal cycle? We answer these questions by focusing on the 10° simulation, as representative of the monsoon-like case, and the 30° simulation, more representative of an ocean-like tropical ITCZ, and by analyzing in detail changes in the circulation and the associated zonal momentum budget throughout the seasonal cycle. We also choose two representative time periods

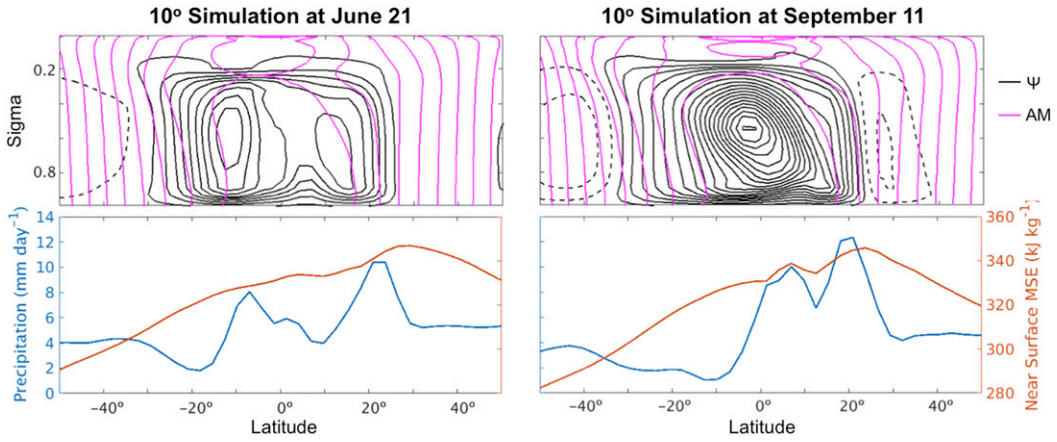

FIG. 6. (top) Total streamfunction Ψ in black (counterclockwise in solid, clockwise in dashed; contour interval: 20 $\times 10^9$ kg s^{-1}) and angular momentum contours in magenta (contour interval: $\Omega a^2/15$) and (bottom) precipitation (blue) and near-surface ($\sigma = 0.887$) MSE distribution (red) from the 10° simulation.

(denoted in Fig. 2), which are 20-day periods centered around two pentads (21 June and 11 September, respectively) that represent different phases of the monsoon development in the 10° simulation: the first pentad captures the initial phase, where local moisture recycling still contributes significantly to continental precipitation; the second pentad, instead, coincides with the peak of the monsoon, when the precipitation is mostly due to the moisture flux convergence by the broad tropical overturning circulation.

In the 10° simulation, prior to the monsoon transition in early NH summer around 21 June, a single strong cross-equatorial circulation cell is not yet established, instead, two smaller circulation cells are observed (top-left panel of Fig. 6). At this time, the AM contours (magenta) are not completely aligned with the streamlines (black) even in the ascending and upper branches, suggesting deviation from AM conservation. The lower-level MSE (bottom-left panel) features one obvious maximum at ~20° and a more subtle maximum at ~10° due to the heating over the coastline during NH spring. This double-maxima MSE structure causes two counterclockwise circulation cells that have precipitation maxima located at the ascending branch of each cell, which explains the double ITCZ structure observed in Fig. 2. By 11 September, a strong broad cross-equatorial winter Hadley cell is established with a weaker summer cell located north of it (top-right panel of Fig. 6). In the upper branch, streamlines are now parallel to the AM contours and the circulation is in the AMC regime. This is the strong tropical summer circulation associated with the monsoon. The rapid movement of the lower-level MSE into subtropical latitudes made possible by the low heat capacity of land (Fig. 2) allows the cross-equatorial circulation to strengthen and expand rapidly. These rapid circulation changes allow for similarly rapid precipitation changes. We also note the existence of a secondary precipitation maximum, located on the summer side of the equator. The secondary precipitation maximum is a very common feature of cross-equatorial circulations in both idealized and realistic simulations (e.g., Privé and Plumb 2007a) and, as detailed in Lobo and Bordoni (2020), coincides with a region where the near-surface meridional temperature gradient changes sign. This result is consistent with the boundary layer dynamics described in Pauluis (2004), by which the flow must jump into the free troposphere in regions where the pressure gradient cannot sustain the required poleward flow.

The results from the 30° simulation (Fig. 7) show a different picture. Around 21 June (left column), the cell structure is more complicated than in the 10° simulation. Two counterclockwise circulations are observed just south of the equator and above the coastline at ~30°, but a smaller clockwise circulation exists between them. The ascending branches of the two counterclockwise cells coincide with the lower-level MSE and precipitation maxima. The upper branches of the overturning cells cross the AM contours, which are essentially vertical. Around 11 September (right column), a broad winter Hadley cell is observed; while distortion of the AM contours from the vertical is seen, the circulation seems to be less efficient at homogenizing AM than the circulation of the 10° case at the same time. Compared to the 10° simulation, the MOC in the 30° simulation extends over regions of larger thermal inertia, which prevents the lower-level MSE from adjusting as rapidly as in the 10° simulation. Hence, the development of a cross-equatorial cell that approaches AM conservation occurs more gradually. This suggests that EMFD influences the circulation strength for a longer part of NH summer, delaying the transition into the AMC regime and preventing the circulation from growing rapidly in strength and extent. In this respect, monsoon-like rapid transitions cannot occur if land remains limited to higher latitudes, as the circulation responds more linearly to the seasonal insolation changes.

To investigate more quantitatively the influence of eddies on the MOC, and the degree to which it approaches the AMC limit, we decompose the total streamfunction Ψ (cf. Schneider and Bordoni 2008) into a component associated with eddy momentum fluxes

$$\Psi_e(\phi, p) = -\frac{2\pi a \cos\phi}{fg}\int_0^p \mathcal{S}\, dp' \tag{5}$$

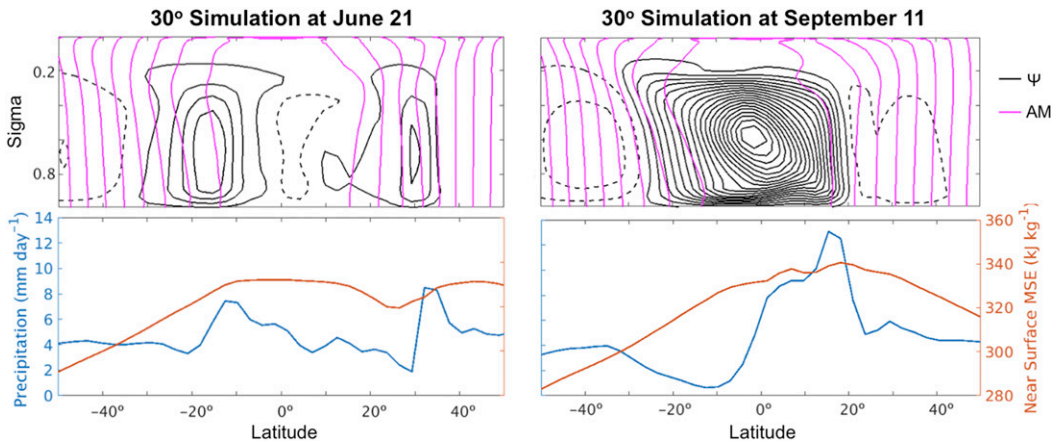

FIG. 7. As in Fig. 6, but from the 30° simulation.

and a component associated with the mean momentum flux

$$\Psi_m(\phi, p) = -\frac{2\pi a \cos\phi}{fg}\int_0^p \mathcal{M}\, dp', \tag{6}$$

where $\mathcal{M}$ is the mean momentum flux divergence. Above the boundary layer where frictional processes can be neglected, $\Psi = \Psi_e + \Psi_m$. Figure 8 shows Ψ_e and Ψ_m (black line) over the EMFD (color) from the 10° and 30° simulations on 21 June and 11 September. In the 10° simulation around 21 June, Ψ_m starts to dominate in both hemispheres as Ψ_e starts to weaken in the subtropics (Fig. 8a). Around 11 September when the monsoonal circulation is broad and strong, Ψ_m clearly dominates globally and has strengthened since 21 June (Fig. 8b). In fact, Ψ_e is only dominant at around 30°S, expanding the extent of the circulation's descending branch in the winter hemisphere. We note that the NH maximum in Ψ_e in the tropics is associated with eddy momentum flux convergence located in the upper troposphere above the Ψ_e maximum. As discussed in previous work, this is indicative of a source of eddy activity (Held 2000), and happens where the absolute vorticity gradient changes sign, a necessary condition for barotropic instability in the cross-equatorial cell (Pedlosky 1964). In the 30° simulation around 21 June, both Ψ_e and Ψ_m are much weaker than those at the same time in the 10° simulation and have equal influence on Ψ (Fig. 8c). Around 11 September, Ψ_m dominates both hemispheres over Ψ_e (Fig. 8d). These results hence show how, once the winter Hadley cell becomes broad and well established, the influence of eddies on the strength of the circulation decreases as the MOC gets closer to the AMC limit. They also demonstrate the importance of having land extend into the tropics to enable the transition into the AMC dynamical regime to occur on a rapid intraseasonal time scale.

The role that tropical land plays in the rapid dynamical regime transition of the MOC becomes more apparent if we look at the seasonal cycle of the terms in the upper-level ($\sigma = 0.195$) zonal momentum budget in Eq. (4) (Fig. 9) and the upper-level zonal wind u_{up} (Fig. 10). The zonal mean Coriolis term $f\,\overline{v}$ is approximately balanced by the sum of the mean flow advection $-(\overline{v}\partial\overline{u}/\partial y + \overline{\omega}\partial\overline{u}/\partial p)$ [note that in Eq. (4) the vertical advection term is neglected] and the eddy momentum flux convergence (EMFC) $-(\partial\overline{u'v'}/\partial y + \partial\overline{u'\omega'}/\partial p)$. In the 10° simulation, during NH summer the poleward extent of the winter Hadley cell rapidly increases starting near 21 June (marked), and gradually retreats after 11 September (marked) around late September (Fig. 4). Simultaneously, over the entire extent of the winter Hadley cell, the magnitude of the zonal mean Coriolis term $|f\overline{v}|$ increases (Fig. 9a), with large negative values in the NH ($f > 0$) and large positive values in the SH ($f < 0$) due to the strong southward flow ($\overline{v} < 0$) over the entire cell. At the same time over the winter Hadley cell, the mean flow advection (Fig. 9b) strongly dominates over the EMFC (Fig. 9c) and approximately balances the Coriolis term. The magnitude of the mean flow advection is especially pronounced in the SH range of the winter Hadley cell. This coincides with a rapid intensification of the upper-level easterlies, which do not support westward-propagating extratropical eddies (Charney 1969; Webster and Holton 1982), over the entire winter Hadley cell during the NH summer (Fig. 10a), in agreement with axisymmetric theories (cf. Lindzen and Hou 1988). The development of the upper-level easterlies in a broad latitudinal range helps shield the winter cell from the eddy influence, which in fact remains confined only to the cell descending branch in the winter hemisphere (Fig. 9c).

In the 30° simulation, the regime transition is delayed and smoother. The expansion of the winter Hadley cell into the NH subtropics is more gradual than observed in the 10° simulation, and occurs later in the season around July (Fig. 4). The circulation not only has a smoother and delayed transition onset, but also does not extend as far poleward (~20°N) as the winter Hadley cell during NH summer in the 10° simulation (~30°N). The effects of the delay and weakening of the transition, as well as the reduced poleward extent of the winter Hadley cell, are observable in the upper-level zonal mean momentum balance (Figs. 9d–f). First, the intensification of the Coriolis term during NH summer is delayed. Simultaneously, the dominance of the mean flow advection over the EMFC is weaker and occurs later in the season in the 30° simulation relative to in the 10°

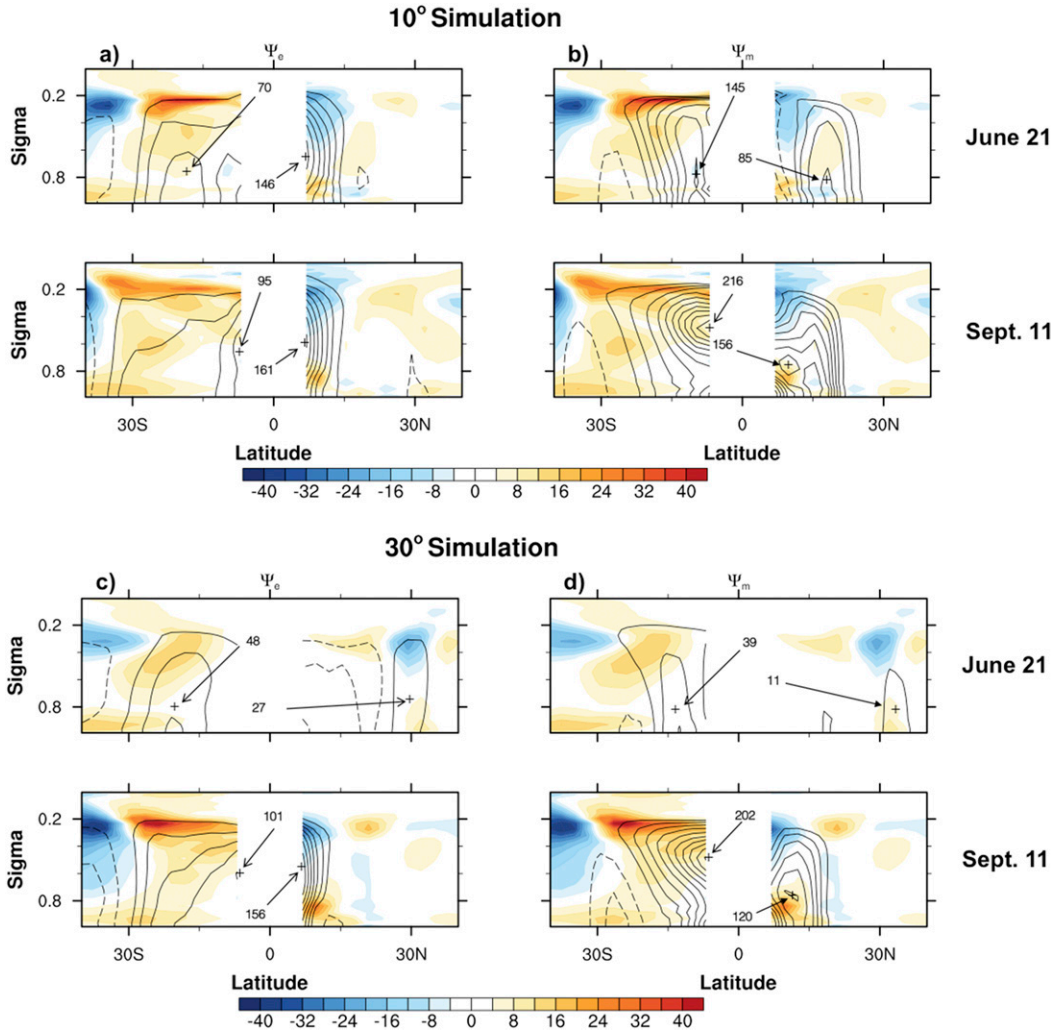

FIG. 8. Decomposition of the total streamfunction Ψ into (left) eddy Ψ_e and (right) mean Ψ_m momentum flux components from simulations with southern boundaries of land at (a),(b) 10° and (c),(d) 30° at (top) 21 Jun and (bottom) 11 Sep. Ψ_e and Ψ_m are in black contours (counterclockwise in solid, clockwise in dashed; contour interval: 20×10^9 kg s^{-1}). The eddy momentum flux divergence is shown in color contours (contour interval: 4×10^{-6} m s^{-2}) and is calculated as $-\nabla \cdot (\overline{p}_s \overline{u'v'}^{\sigma} \cos\phi)/\overline{p}_s$, where $\overline{p}_s$ is the zonal- and temporal-mean surface pressure, $\overline{(\cdot)}^{\sigma}$ is a surface pressure–weighted zonal and temporal mean along sigma surfaces, and $(\cdot)'$ indicates deviations from the mean. The NH and SH maxima in both Ψ_e and Ψ_m are given in 10^9 kg s^{-1} and marked by the arrows.

simulation. Additionally, the onset of the strengthening of the upper-level easterlies is also delayed in the 30° simulation (~July, Fig. 10b) compared to the 10° simulation (~June, Fig. 10a) and their peak amplitude is much weaker (21.9 vs 60.2 m s^{-1}). The weakening and delay of the intensification of upper-level easterlies, as well as their reduced meridional extent, delay the timing and limit the latitudinal range over which they can effectively shield the tropical circulation from the extratropical eddies. This emphasizes that, while the tropical circulation eventually approaches the AMC regime in the 30° simulation, it does so later in the season. Overall, these results demonstrate that having land in the tropics can influence the monsoon onset mainly through enabling the circulation to switch rapidly from the regime where its strength is tied to the extratropical baroclinic eddies to the monsoon regime where it approaches the AMC limit. Tropical land is hence necessary for the development of strong monsoons with a rapid onset in so far as it provides a lower boundary with heat capacity that is low enough to allow for rapid near-surface MSE adjustments that initiate the dynamical feedbacks described above.

b. *Vorticity budget perspective*

The dynamics of rapid monsoon transitions have recently been reinterpreted by Geen et al. (2018) in terms of the upper-level vorticity budget. Additional analyses of the upper-level vorticity budget hence provide an alternative and complementary perspective on the dynamics of monsoon transitions to that from the AM budget. Hence, in this section we analyze the

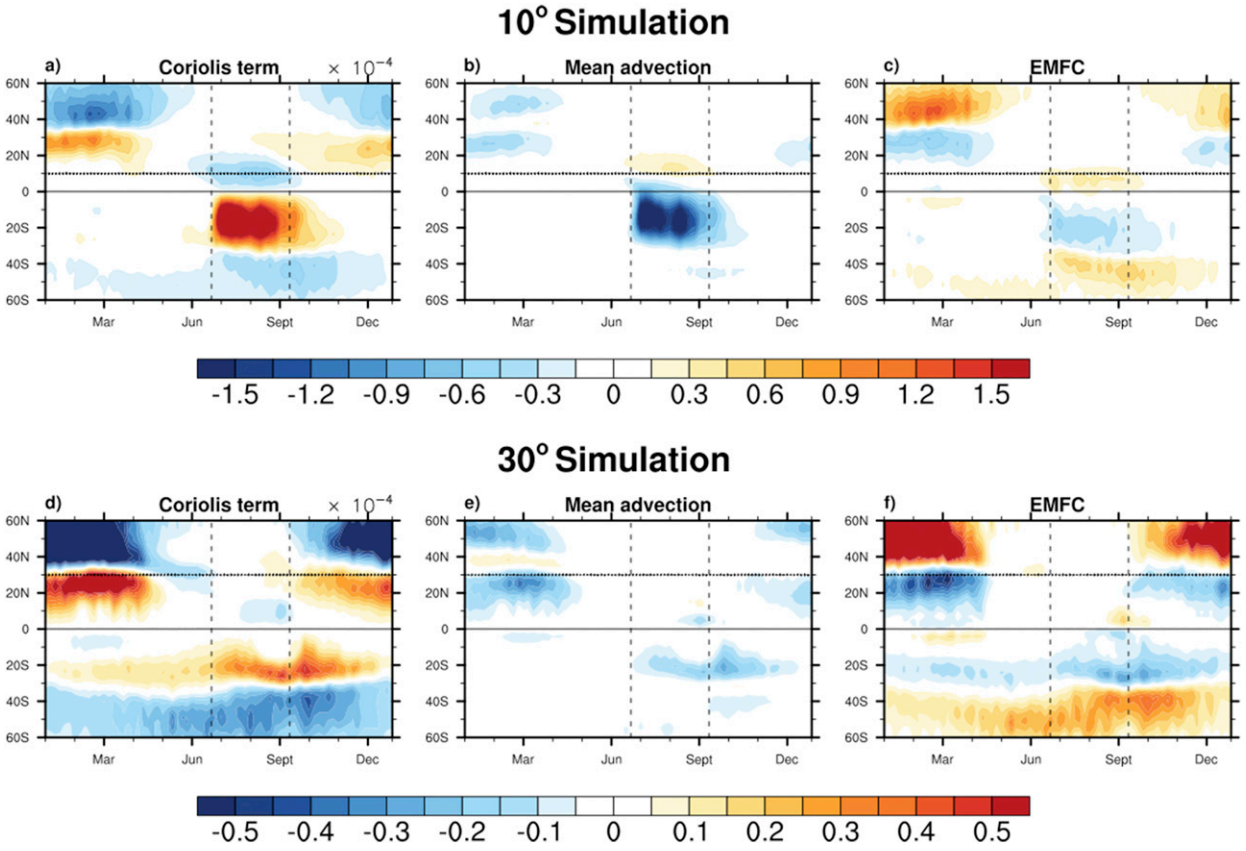

FIG. 9. Seasonal cycle of the terms in the upper-level ($\sigma = 0.195$) zonal momentum budget in Eq. (4): (a) zonal mean Coriolis term $f\overline{v}$, (b) mean-flow advection $-(\overline{v}\partial\overline{u}/\partial y + \overline{\omega}\partial\overline{u}/\partial p)$, and (c) transient eddy momentum flux convergence $-(\partial\overline{u'v'}/\partial y + \partial\overline{u'\omega'}/\partial p)$ from the 10° simulation with a contour interval of 1.5×10^{-5} m s^{-2}, and (d)–(f) as in (a)–(c), but from the 30° simulation with a contour interval of 0.5×10^{-5} m s^{-2}. Vertical dashed lines mark 21 Jun and 11 Sep and the horizontal dotted line represents the continent southern coastline.

seasonal cycle of the different terms in the vorticity budget, given by

$$\frac{\partial\zeta}{\partial t} = -\mathbf{u}\cdot\nabla(\zeta+f) - \omega\frac{\partial\zeta}{\partial p} - (\zeta+f)\nabla\cdot\mathbf{u} + \mathbf{k}\cdot\left(\frac{\partial\mathbf{u}}{\partial p}\times\nabla\omega\right). \tag{7}$$

The vorticity tendency on the left-hand side is balanced by the horizontal vorticity advection, the vertical vorticity advection, vortex stretching, and vortex tilting on the right-hand side. In the upper troposphere where ω is small, and the terms with ω are small compared to the horizontal advection and vortex stretching terms, Eq. (7) simplifies to

$$\frac{\partial\overline{\zeta}}{\partial t} = -\overline{v}\frac{\partial(\overline{\zeta}+f)}{\partial y} - (\overline{\zeta}+f)\frac{\partial\overline{v}}{\partial y}. \tag{8}$$

Throughout the season, hence the horizontal advection and vortex stretching terms act as tendencies of the upper-level absolute vorticity via changes in $\overline{\zeta}$ (Geen et al. 2018). Remembering that the upper-level absolute vorticity $f + \overline{\zeta}$ is proportional to the meridional gradient of M, a circulation with R_o approaching 1 has vanishing absolute vorticity in its upper branch (Schneider 2006; Geen et al. 2018).

Geen et al. (2018) proposed that, at the onset of NH summer as the ITCZ crosses the equator, simultaneously the horizontal advection tendency becomes positive and the vortex stretching tendency becomes negative in the summer hemisphere. This results in a latitudinally broad region of reduced magnitude of absolute vorticity and, hence, AM conservation. They also showed that the positive horizontal advection tendency results from southward flow in the winter cell's upper branch in NH summer, which increases (decreases) absolute vorticity in the summer (winter) hemisphere by advecting higher absolute vorticity air downgradient. The divergent flow in the ascending branch of the Hadley cell instead contributes a negative vortex stretching tendency.

The seasonal evolution of the upper-level horizontal advection and vortex stretching tendencies calculated from our 10° simulation bear similarity to those described in Geen et al. (2018) (Fig. 11). Focusing on the transition into NH summer, from the time the ITCZ crosses the equator before NH summer in May till the end of NH summer in September, from near the equator in the SH up to the winter Hadley cell poleward edge near 25°N is a region of reduced magnitude of absolute vorticity, as the circulation becomes more AMC (Fig. 11f). This results from the combined effect of positive horizontal

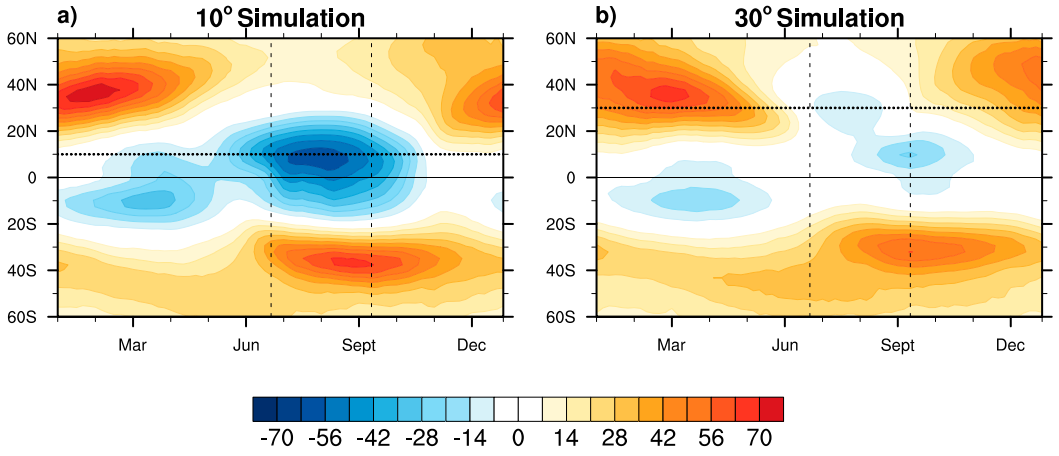

FIG. 10. Seasonal cycles of upper-level ($\sigma = 0.195$) zonal wind u_{up} (contour interval: 7 m s^{-1}) from the (a) 10° and (b) 30° simulations. Vertical dashed lines mark 21 Jun and 11 Sep and the horizontal dotted line represents the continent southern coastline.

advection of vorticity (Fig. 11a) and negative vortex stretching (Fig. 11d), whose sum is shown in Fig. 13a. Over most of the meridional range of the winter Hadley cell from 30°S up to the coastline at 10°N, the horizontal advection term is positive, because of the southward mean flow and positive meridional gradient of absolute vorticity in this region, and results in a decrease in the magnitude of the negative absolute vorticity in the SH. At the same time, the vortex stretching tendency is negative from the equator up to ~30°N due to the divergent flow in the circulation's ascending branch and the positive magnitude of the absolute vorticity in this region. The combined effect (Fig. 13a) is the observed reduction in magnitude and meridional gradient of absolute vorticity across the winter Hadley cell from May through September (Fig. 11f). We do note that during NH summer there is a region of negative horizontal advection tendency around the coastline at 10°N. This results from a negative meridional gradient in vorticity over the same latitude (Fig. 11b), as discussed in the previous section. However, since the positive horizontal advection mainly works to reduce the magnitude of negative absolute vorticity in the SH, this patch of negative horizontal advection at the coastline does not affect the overall influence of the horizontal vorticity advection.

Geen et al. (2018) also suggest that the monsoon regime transitions coincide with peaks in the horizontal advection and vortex stretching tendencies. As the ascending branch of the

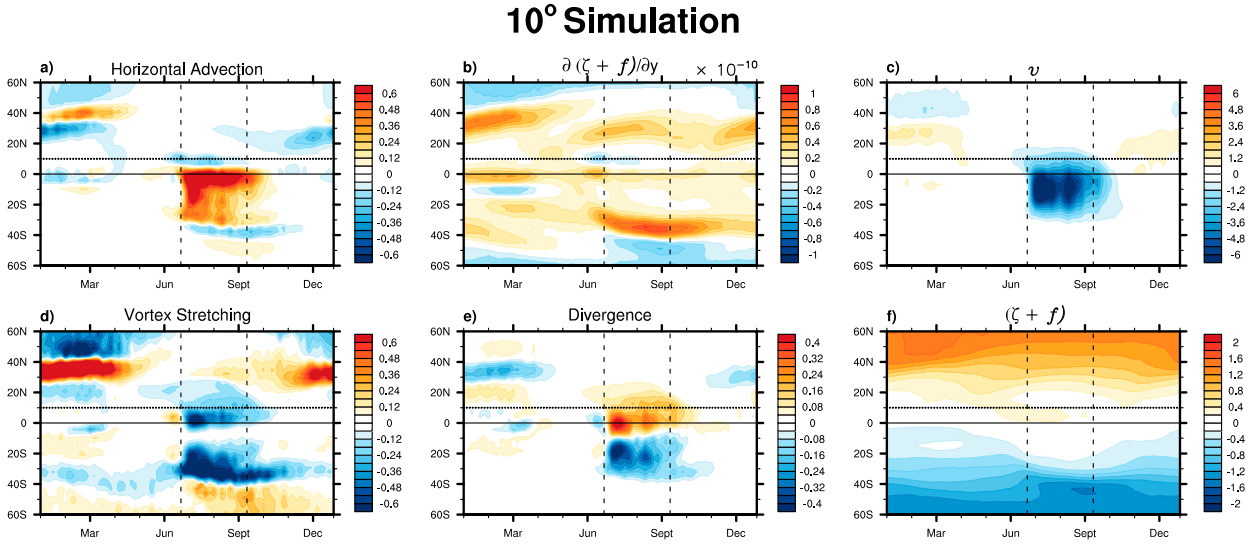

FIG. 11. Seasonal cycle and decomposition of terms in the vorticity budget in Eq. (7) from the 10° simulation at $\sigma = 0.195$: (a) $-\mathbf{u} \cdot \nabla(\bar{\zeta} + f)$ (contour interval: 0.06 day^{-2}), (b) $\partial(\bar{\zeta} + f)/\partial y$ (contour interval: 0.1×10^{-10} m^{-1} s^{-1}), (c) $\bar{v}$ (contour interval: 0.6 m s^{-1}), (d) $-(\bar{\zeta} + f)\nabla \cdot \bar{\mathbf{u}}$ (contour interval: 0.06 day^{-2}), (e) $\nabla \cdot \bar{\mathbf{u}}$ (contour interval: 0.04 day^{-1}), and (f) $\bar{\zeta} + f$ (contour interval: 0.2 day^{-1}). Vertical dashed lines mark 21 Jun and 11 Sep and the horizontal dotted line represents the continent southern coastline.

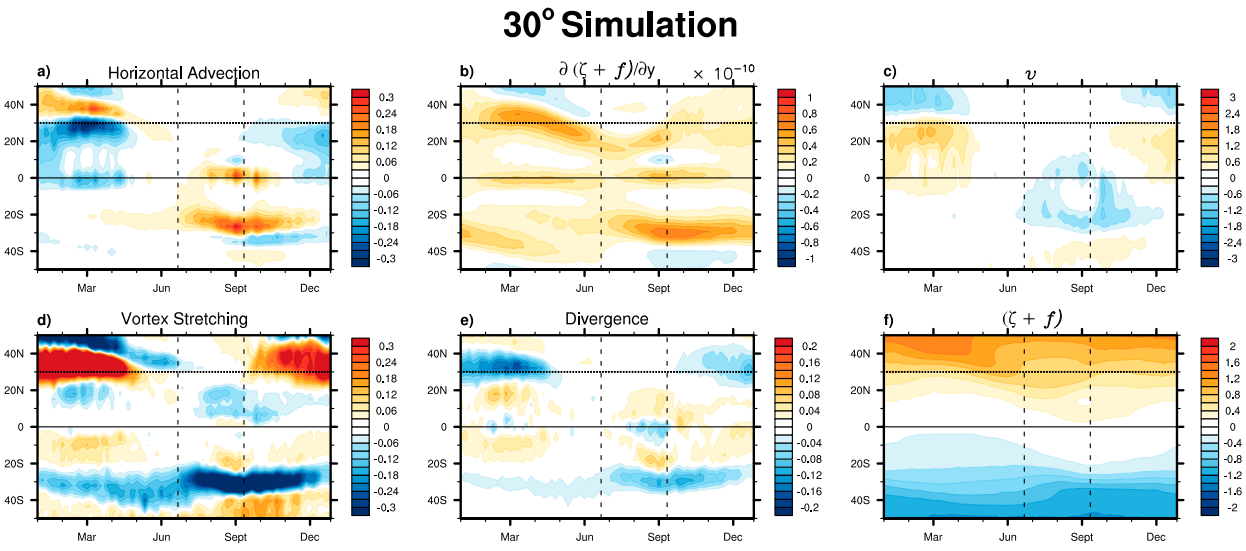

FIG. 12. As in Fig. 11, but from the 30° simulation and contour intervals are (a) 0.03 day^{-2}, (b) 0.1 × 10^{-10} m^{-1} s^{-1}, (c) 0.3 m s^{-1}, (d) 0.03 day^{-2}, (e) 0.02 day^{-1}, and (f) 0.2 day^{-1}.

Hadley circulation and peak in divergent flow move poleward during NH summer, they move from a region with near zero absolute vorticity near the equator to a region of nonnegligible absolute vorticity, resulting in a rapid increase in the negative vortex stretching. The link between the peaks in the tendencies and the dynamical regime transition is observable in our 10° simulation: these peaks are in fact observed immediately following 21 June, after which the extratropical eddies' influence on the MOC is weakened and the MOC transitions into the AMC limit. While lagging the cross-equatorial jump of the ITCZ more than in the full aquaplanet simulation with 2 m MLD in Geen et al. (2018), these peaks do appear to coincide with the rapid growth in strength and poleward extent of the overturning cell.

Compared to the 10° simulation, the changes in horizontal advection and vortex stretching tendencies in the 30° simulation are relatively smooth and delayed (Fig. 12). During NH summer, the positive horizontal advection (Fig. 12a) over the winter Hadley cell has a greatly reduced magnitude compared to that in the 10° simulation (Fig. 11a), because of a much weaker MOC (cf. Fig. 11c to Fig. 12c). The region of negative vortex stretching during NH summer also extends less poleward and is less strongly negative in the 30° simulation (Fig. 12d) than that in the 10° simulation (Fig. 11d). These are results of a weaker and narrower winter Hadley cell in the 30° simulation, resulting in weaker horizontal divergence (Fig. 12e). Consequently, in the 30° simulation during NH summer the combined effect of the horizontal advection and vortex stretching terms (sum shown in Fig. 13b) does not reduce the absolute vorticity in the NH subtropics (Fig. 12f) as effectively as in the 10° simulation (Fig. 11f), confirming the slower transition into the AMC limit in this case. Additionally, at the start of NH summer there are

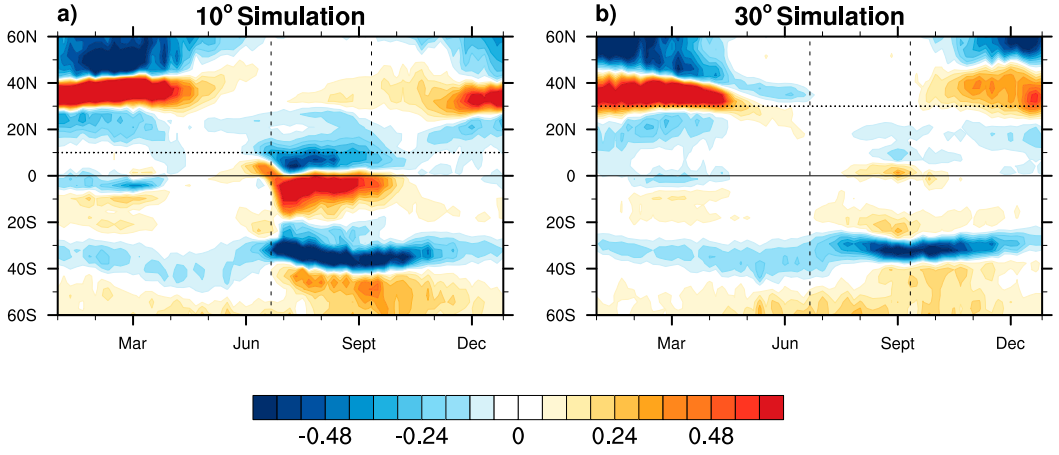

FIG. 13. Total vorticity tendency (sum of the vortex stretching and horizontal advection tendencies from Figs. 11 and 12; contour interval: 0.06 day^{-2}).

no significant peaks or rapid changes in the horizontal advection and vortex stretching tendencies as observed in the 10° simulation, reflecting the more slowly evolving dynamics in the simulation with land confined to higher latitudes. This is also apparent in the very smooth evolution of the zero contour of the absolute vorticity (Fig. 11f). From the perspective of the vorticity budget, having land in the tropics enables the dynamical monsoon regime transition to occur on a rapid intraseasonal time scale by rapidly strengthening the divergent flow of the Hadley circulation as its ascending branch moves poleward to regions of nonnegligible absolute vorticity, to quickly increase the magnitude of the vortex stretching term and of the horizontal vorticity advection, which efficiently reduce the magnitude of the absolute vorticity and decouple the circulation from the eddy momentum fluxes.

5. Discussion

The complementary interpretations of the dynamical monsoon regime transition presented in the previous section are tied together by the migration of the ascending branch of the Hadley circulation, both in terms of the direct effect of the eddy momentum fluxes on the streamfunction (Figs. 8 and 9) and the seasonal evolution of absolute vorticity (Figs. 11 and 12). A more poleward migration of the ascending branch widens the winter cell's poleward extent in both hemispheres and extends the region of prevalent upper-level easterlies within the tropical circulation into a broad latitudinal band in both the summer and winter hemisphere. This helps diminish the influence of the strength of the extratropical eddies originating in the winter hemisphere on the tropical circulation by shielding the circulation and weakening the EMFD at the cell center, and therefore enables the circulation to approach the AMC limit and become more thermally driven and rapidly strengthen. A more poleward migration of the ascending branch also brings the region of strongest upper-level horizontal divergence to a region of higher absolute vorticity in the NH and strongest horizontal advection to a region of large negative magnitude of absolute vorticity in the SH, since the positive meridional gradient of absolute vorticity in the NH increases with latitude. This in turn increases the vortex stretching and horizontal advection tendencies and results in a more efficient reduction of absolute vorticity across the entire winter Hadley cell and therefore a more AMC circulation. Regardless through which interpretation, once the circulation approaches the AMC limit and becomes more thermally driven, the cell can grow rapidly in strength and extent through two dynamical feedbacks—1) by advecting lower MSE air in its lower branch from the winter to the summer hemisphere, enabling the circulation to push the near-surface MSE maximum increasingly poleward and strengthen the temperature gradient, which by AM conservation requires a strengthening of the flow (Fig. 6); and 2) by also strengthening the upper-level easterlies in the winter hemisphere, effectively shielding the winter cell from the influence of the extratropical eddies and allowing it to more closely approach the AMC limit and further strengthen the upper-level easterlies (Figs. 9 and 10) (Schneider and Bordoni 2008).

It is through this key ingredient—a significant off-equatorial migration of the ascending branch of the Hadley circulation—that continental geometry appears to play an important role for the monsoon. By having more land or regions of low thermal inertia in the tropics, the distribution of the near-surface MSE can evolve rapidly, and the nonlinear mechanisms described above help push its maximum far enough away from the equator into the subtropics for the circulation to grow rapidly in strength and extent. Only when these nonlinear mechanisms can operate on intraseasonal time scales, can a rapid monsoon onset be seen in our simulations.

We conclude this section with a brief remark on the temporal asymmetry between a rapid onset and a more gradual retreat that appears particularly evident in the simulations with continents extending to tropical latitudes. Such an asymmetry was also observed to occur in aquaplanet simulations reported by Geen et al. (2019), who attributed it to changes in SSTs induced by the wind-induced surface heat exchange (WISHE) feedback (Emanuel 1987; Neelin et al. 1987). More specifically, they argue that WISHE slows the monsoon withdrawal through weak lower-level horizontal winds below the ITCZ, which keep the latent heat flux from the surface low and the SSTs warm below the ITCZ as it retreats to the winter hemisphere. Evidence of a slight temporal asymmetry between onset and withdrawal is also seen in the all-land (not shown) and all-ocean aquaplanet simulations (Fig. 2). It is however clear that a large hemispheric asymmetry in lower-boundary thermal inertia gives rise to a more pronounced asymmetry in the monsoon temporal evolution: in the presence of a continent at tropical latitudes, the lower-level MSE can adjust rapidly as the circulation transitions into the monsoon regime. As the circulation retreats from the summer hemisphere and its ascending branch moves over the ocean, its large heat capacity instead prevents rapid MSE changes, hence slowing down the withdrawal phase. We believe that the hemispheric asymmetry in the lower-boundary thermal inertia might be a more relevant mechanism than the WISHE feedback for the temporal asymmetry of observed monsoons. More targeted simulations, in which for instance the WISHE feedback is disabled, will shed further light into these open questions.

6. Conclusions

Altogether, this study aims to understand how changing continental geometry can affect the spatial and temporal structure of the monsoonal precipitation. Five simulations are analyzed in an idealized aquaplanet GCM, where hemispheric asymmetry in thermal inertia is varied by using different continental configurations with zonally symmetric land extending poleward from southern boundaries at 0°, 10°, 20°, 30°, and 40°. From studying the seasonal cycles of precipitation, near-surface MSE, mass streamfunction, and horizontal winds, we find that only the 0°, 10°, and 20° simulations with land extending into the lower latitudes have circulation and precipitation changes characteristic of observed monsoons. By breaking down the streamfunction into eddy and mean components and analyzing the seasonal cycle of the upper-level zonal momentum budget, our simulations suggest that

different continental geometry can affect the spatial and temporal structure of the circulation and precipitation by affecting the circulation's ability to transition rapidly from a regime where the tropical circulation strength is controlled by eddy momentum fluxes to a regime where the strength is more directly controlled by energetic constraints. Having regions of low thermal inertia in the tropics enables this transition to occur on an intraseasonal scale; in contrast without land in the low latitudes, the circulation transitions are smoother and less similar to those seen in observed monsoons. This is because having land in the tropics allows the near-surface MSE maximum, and with it the ascending branch of the Hadley circulation, to adjust rapidly, allowing internal dynamical feedbacks to operate and to rectify the response to the smooth insolation forcing into a rapid onset.

That experiments with such idealized physics and configuration can replicate important features of the observed large-scale monsoons suggests the robustness of the underlying dynamics. It is however important to highlight the limitations in our study. First, in our simulations even land surfaces are completely saturated. In fact, at the beginning of the warm season, our simulations feature continental precipitation that is primarily driven by local evaporation, rather than moisture flux convergence. This is of course an artifact of our choice of a saturated continent and would be prevented to occur if a more realistic land surface hydrology scheme were used, with expected impacts on the timing of monsoon onset (Cook and Gnanadesikan 1991; Peyrillé et al. 2016). Other limitations include the absence of important radiative feedbacks, such as those associated with water vapor and cloud feedbacks, and the lack of albedo contrast between land and ocean, and any zonal asymmetry (Maroon and Frierson 2016; Maroon et al. 2016). Additionally, we prescribe a zonally symmetric OHT, that neglects possible seasonality in the amplitude and direction of OHT in response to changing surface wind (Kang et al. 2018; Lutsko et al. 2019). Future work will be aimed at progressively including these effects, bridging the gap between our idealized simulations and those with comprehensive Earth system models and observations.

Acknowledgments. This work was supported by the National Science Foundation (AGS-1462544) and Caltech's Terrestrial Hazards Observation and Reporting (THOR) Center. We thank three anonymous reviewers, whose comments greatly improved the manuscript.

REFERENCES

Adam, O., T. Bischoff, and T. Schneider, 2016: Seasonal and interannual variations of the energy flux equator and ITCZ. Part II: Zonally varying shifts of the ITCZ. *J. Climate*, **29**, 7281–7293, https://doi.org/10.1175/JCLI-D-15-0710.1.

Biasutti, M., and Coauthors, 2018: Global energetics and local physics as drivers of past, present and future monsoons. *Nat. Geosci.*, **11**, 392–400, https://doi.org/10.1038/s41561-018-0137-1.

Bischoff, T., and T. Schneider, 2014: Energetic constraints of the position of the intertropical convergence zone. *J. Climate*, **27**, 4937–4951, https://doi.org/10.1175/JCLI-D-13-00650.1.

Boos, W. R., and Z. Kuang, 2010: Dominant control of the South Asian monsoon by orographic insulation versus plateau heating. *Nature*, **463**, 218–222, https://doi.org/10.1038/nature08707.

——, and R. L. Korty, 2016: Regional energy budget control of the intertropical convergence zone and application to mid-Holocene rainfall. *Nat. Geosci.*, **9**, 892–897, https://doi.org/10.1038/ngeo2833.

Bordoni, S., and T. Schneider, 2008: Monsoons as eddy-mediated regime transitions of the tropical overturning circulation. *Nat. Geosci.*, **1**, 515–519, https://doi.org/10.1038/ngeo248.

Charney, J., 1969: A further note on large-scale motions in the tropics. *J. Atmos. Sci.*, **26**, 182–185, https://doi.org/10.1175/1520-0469(1969)026<0182:AFNOLS>2.0.CO;2.

Chou, C., and J. D. Neelin, 2004: Mechanisms of global warming impacts on regional tropical precipitation. *J. Climate*, **17**, 2688–2701, https://doi.org/10.1175/1520-0442(2004)017<2688:MOGWIO>2.0.CO;2.

——, ——, and H. Su, 2001: Ocean-atmosphere-land feedbacks in an idealized monsoon. *Quart. J. Roy. Meteor. Soc.*, **127**, 1869–1891, https://doi.org/10.1002/qj.49712757602.

Collins, M., and Coauthors, 2018: Challenges and opportunities for improved understanding of regional climate dynamics. *Nat. Climate Change*, **8**, 101–108, https://doi.org/10.1038/s41558-017-0059-8.

Cook, K. H., and A. Gnanadesikan, 1991: Effects of saturated and dry land surfaces on the tropical circulation and precipitation in a general circulation model. *J. Climate*, **4**, 873–889, https://doi.org/10.1175/1520-0442(1991)004<0873:EOSADL>2.0.CO;2.

Dirmeyer, P. A., 1998: Land-sea geometry and its effect on monsoon circulations. *J. Geophys. Res.*, **103**, 11 555–11 572, https://doi.org/10.1029/98JD00802.

Emanuel, K. A., 1987: An air–sea interaction model of intraseasonal oscillations in the tropics. *J. Atmos. Sci.*, **44**, 2324–2340, https://doi.org/10.1175/1520-0469(1987)044<2324:AASIMO>2.0.CO;2.

——, 1995: On thermally direct circulations in moist atmospheres. *J. Atmos. Sci.*, **52**, 1529–1534, https://doi.org/10.1175/1520-0469(1995)052<1529:OTDCIM>2.0.CO;2.

——, J. D. Neelin, and C. Bretherton, 1994: On large-scale circulations in convecting atmospheres. *Quart. J. Roy. Meteor. Soc.*, **120**, 1111–1143, https://doi.org/10.1002/qj.49712051902.

Flohn, H., 1957: Large-scale aspects of the summer monsoon in South and East Asia. *J. Meteor. Soc. Japan*, **35A**, 180–186, https://doi.org/10.2151/jmsj1923.35A.0_180.

Frierson, D. M. W., 2007: The dynamics of idealized convection schemes and their effect on the zonally averaged tropical circulation. *J. Atmos. Sci.*, **64**, 1959–1976, https://doi.org/10.1175/JAS3935.1.

——, I. M. Held, and P. Zurita-Gotor, 2006: A gray-radiation aquaplanet moist GCM. Part I: Static stability and eddy scales. *J. Atmos. Sci.*, **63**, 2548–2566, https://doi.org/10.1175/JAS3753.1.

Geen, R., F. Lambert, and G. Vallis, 2018: Regime change behavior during Asian monsoon onset. *J. Climate*, **31**, 3327–3348, https://doi.org/10.1175/JCLI-D-17-0118.1.

——, ——, and ——, 2019: Processes and timescales in onset and withdrawal of "aquaplanet monsoons." *J. Climate*, **76**, 2357–2373, https://doi.org/10.1175/JAS-D-18-0214.1.

Held, I. M., 2000: The general circulation of the atmosphere. *Proc. Program in Geophysical Fluid Dynamics*, Woods Hole, MA, Woods Hole Oceanography Institution.

——, and A. Y. Hou, 1980: Nonlinear axially symmetric circulations in a nearly inviscid atmosphere. *J. Atmos. Sci.*, **37**, 515–533,

https://doi.org/10.1175/1520-0469(1980)037<0515:NASCIA>2.0.CO;2.

Hill, S. A., 2019: Theories for past and future monsoon rainfall changes. *Curr. Climate Change Rep.*, **5**, 160–171, https://doi.org/10.1007/s40641-019-00137-8.

Jeevanjee, N., P. Hassanzadeh, S. Hill, and A. Sheshadri, 2017: A perspective on climate model hierarchies. *J. Adv. Model. Earth Syst.*, **9**, 1760–1771, https://doi.org/10.1002/2017MS001038.

Kang, S. M., D. M. W. Frierson, and M. Zhao, 2008: The response of the ITCZ to extratropical thermal forcing: Idealized slab-ocean experiments with a GCM. *J. Climate*, **21**, 3521–3532, https://doi.org/10.1175/2007JCLI2146.1.

——, ——, and I. M. Held, 2009: The tropical response to extratropical thermal forcing in an idealized GCM: The importance of radiative feedbacks and convective parameterization. *J. Atmos. Sci.*, **66**, 2812–2827, https://doi.org/10.1175/2009JAS2924.1.

——, Y. Shin, and S.-P. Xie, 2018: Extratropical forcing and tropical rainfall distribution: Energetics framework and ocean Ekman advection. *npj Climate Atmos. Sci.*, **1**, 20172, https://doi.org/10.1038/s41612-017-0004-6.

Laraia, A., 2015: Observations and modeling of tropical planetary atmospheres. Ph.D. thesis, Environmental Science and Engineering, California Institute of Technology, 76 pp.

Lindzen, S. R., and A. Y. Hou, 1988: Hadley circulations for zonally averaged heating centered off the equator. *J. Atmos. Sci.*, **45**, 2416–2427, https://doi.org/10.1175/1520-0469(1988)045<2416:HCFZAH>2.0.CO;2.

Lobo, A. H., and S. Bordoni, 2020: Atmospheric dynamics of high obliquity planets. *Icarus*, **340**, 115391, https://doi.org/10.1016/J.ICARUS.2019.113592.

Lutsko, N. J., J. Marshall, and B. Green, 2019: Modulation of monsoon circulations by cross-equatorial ocean heat transport. *J. Climate*, **32**, 3471–3485, https://doi.org/10.1175/JCLI-D-18-0623.1.

Maroon, E. A., and D. M. W. Frierson, 2016: The impact of a continent's longitudinal extent on tropical precipitation. *Geophys. Res. Lett.*, **43**, 11 921–11 929, https://doi.org/10.1002/2016GL071518.

——, ——, S. M. Kang, and J. Scheff, 2016: The precipitation response to an idealized subtropical continent. *J. Climate*, **29**, 4543–4564, https://doi.org/10.1175/JCLI-D-15-0616.1.

Merlis, T., T. Schneider, S. Bordoni, and I. Eisenman, 2013: Hadley circulation response to orbital precession. Part II: Subtropical continent. *J. Climate*, **26**, 754–771, https://doi.org/10.1175/JCLI-D-12-00149.1.

Molnar, P., W. R. Boos, and D. S. Battisti, 2010: Orographic controls on climate and paleoclimate of Asia: Thermal and mechanical roles for the Tibetan Plateau. *Annu. Rev. Earth Planet. Sci.*, **38**, 77–102, https://doi.org/10.1146/annurev-earth-040809-152456.

Neelin, J. D., 2007: Moist dynamics of tropical convection zones in monsoons, teleconnections and global warming. *The Global Circulation of the Atmosphere*, Princeton University Press, 267–301.

——, and I. M. Held, 1987: Modeling tropical convergence based on the moist static energy budget. *Mon. Wea. Rev.*, **115**, 3–12, https://doi.org/10.1175/1520-0493(1987)115<0003:MTCBOT>2.0.CO;2.

——, ——, and K. H. Cook, 1987: Evaporation–wind feedback and low-frequency variability in the tropical atmosphere. *J. Atmos. Sci.*, **44**, 2341–2348, https://doi.org/10.1175/1520-0469(1987)044<2341:EWFALF>2.0.CO;2.

O'Gorman, P. A., and T. Schneider, 2008: The hydrological cycle over a wide range of climates simulated with an idealized GCM. *J. Climate*, **21**, 3815–3832, https://doi.org/10.1175/2007JCLI2065.1.

Pauluis, O., 2004: Boundary layer dynamics and cross-equatorial Hadley circulation. *J. Atmos. Sci.*, **61**, 1161–1173, https://doi.org/10.1175/1520-0469(2004)061<1161:BLDACH>2.0.CO;2.

Pedlosky, J., 1964: The stability of currents in the atmosphere and the ocean: Part I. *J. Atmos. Sci.*, **21**, 201–219, https://doi.org/10.1175/1520-0469(1964)021<0201:TSOCIT>2.0.CO;2.

Peyrillé, P., J.-P. Lafore, and A. Boone, 2016: The annual cycle of the West African monsoon in a two-dimensional model: Mechanisms of the rain-band migration. *Quart. J. Roy. Meteor. Soc.*, **142**, 1473–1489, https://doi.org/10.1002/qj.2750.

Plumb, R. A., and A. Y. Hou, 1992: The response of a zonally symmetric atmosphere to subtropical thermal forcing: Threshold behavior. *J. Atmos. Sci.*, **49**, 1790–1799, https://doi.org/10.1175/1520-0469(1992)049<1790:TROAZS>2.0.CO;2.

Popp, M., and N. J. Lutsko, 2017: Quantifying the zonal-mean structure of tropical precipitation. *Geophys. Res. Lett.*, **44**, 9470–9478, https://doi.org/10.1002/2017GL075235.

Privé, N. C., and R. A. Plumb, 2007a: Monsoon dynamics with interactive forcing. Part I: Axisymmetric studies. *J. Atmos. Sci.*, **64**, 1417–1430, https://doi.org/10.1175/JAS3916.1.

Schneider, T., 2006: The general circulation of the atmosphere. *Annu. Rev. Earth Planet. Sci.*, **34**, 655–688, https://doi.org/10.1146/annurev.earth.34.031405.125144.

——, and S. Bordoni, 2008: Eddy-mediated regime transitions in the seasonal cycle of a Hadley circulation and implications for monsoon dynamics. *J. Atmos. Sci.*, **65**, 915–934, https://doi.org/10.1175/2007JAS2415.1.

——, T. Bischoff, and G. H. Haug, 2014: Migrations and dynamics of the intertropical convergence zone. *Nature*, **513**, 45–53, https://doi.org/10.1038/nature13636.

Voigt, A., and Coauthors, 2016: The Tropical Rain belts with an Annual cycle and a Continent Model Intercomparison Project: TRACMIP. *J. Adv. Model. Earth Syst.*, **8**, 1868–1891, https://doi.org/10.1002/2016MS000748.

Walker, C., and T. Schneider, 2006: Eddy influences on Hadley circulations: Simulations with an idealized GCM. *J. Atmos. Sci.*, **63**, 3333–3350, https://doi.org/10.1175/JAS3821.1.

Walker, J. M., 2017: Seasonal and interannual variability in South Asian monsoon dynamics. Ph.D. thesis, California Institute of Technology, 121 pp.

——, and S. Bordoni, 2016: Onset and withdrawal of the large-scale South Asian monsoon: A dynamical definition using change point detection. *Geophys. Res. Lett.*, **43**, 11 815–11 822, https://doi.org/10.1002/2016GL071026.

Webster, P., and J. Holton, 1982: Cross-equatorial response to middle-latitude forcing in a zonally varying basic state. *J. Atmos. Sci.*, **39**, 722–733, https://doi.org/10.1175/1520-0469(1982)039<0722:CERTML>2.0.CO;2.

Xie, S., and N. Saiki, 1999: Abrupt onset and slow seasonal evolution of summer monsoon in an idealized GCM simulation. *J. Meteor. Soc. Japan*, **77**, 949–968, https://doi.org/10.2151/jmsj1965.77.4_949.

Zhou, W., and S.-P. Xie, 2018: A hierarchy of idealized monsoons in an intermediate GCM. *J. Climate*, **31**, 9021–9036, https://doi.org/10.1175/JCLI-D-18-0084.1.